March 2002

Imaging mechanism of piezoresponse force microscopy of ferroelectric surfaces

Sergei V. Kalinin
University of Pennsylvania

Dawn A. Bonnell
University of Pennsylvania, bonnell@lrsm.upenn.edu

Copyright American Physical Society. Reprinted from *Physical Review B*, Volume 65, Issue 12, Article Number 125408, 15 March 2002, 11 pages.
Publisher URL: http://dx.doi.org/10.1103/PhysRevB.65.125408

Imaging mechanism of piezoresponse force microscopy of ferroelectric surfaces

Abstract

In order to determine the origin of image contrast in piezoresponse force microscopy (PFM), analytical descriptions of the complex interactions between a small tip and ferroelectric surface are derived for several sets of limiting conditions. Image charge calculations are used to determine potential and field distributions at the tip-surface junction between a spherical tip and an anisotropic dielectric half plane. Methods of Hertzian mechanics are used to calculate the response amplitude in the electrostatic regime. In the electromechanical regime, the limits of strong (classical) and weak (field-induced) indentation are established and the relative contributions of electroelastic constants are determined. These results are used to construct "piezoresponse contrast mechanism maps" that correlate the imaging conditions with the PFM contrast mechanisms. Conditions for quantitative PFM imaging are set forth. Variable-temperature PFM imaging of domain structures in $BaTiO_3$ and the temperature dependence of the piezoresponse are compared with Ginzburg-Devonshire theory. An approach to the simultaneous acquisition of piezoresponse and surface potential images is proposed.

Publisher URL: http://dx.doi.org/10.1103/PhysRevB.65.125408

Imaging mechanism of piezoresponse force microscopy of ferroelectric surfaces

Sergei V. Kalinin and Dawn A. Bonnell
Department of Materials Science and Engineering, University of Pennsylvania, 3231 Walnut Street, Philadelphia, Pennsylvania 19104
(Received 10 August 2001; published 11 March 2002)

In order to determine the origin of image contrast in piezoresponse force microscopy (PFM), analytical descriptions of the complex interactions between a small tip and ferroelectric surface are derived for several sets of limiting conditions. Image charge calculations are used to determine potential and field distributions at the tip-surface junction between a spherical tip and an anisotropic dielectric half plane. Methods of Hertzian mechanics are used to calculate the response amplitude in the electrostatic regime. In the electromechanical regime, the limits of strong (classical) and weak (field-induced) indentation are established and the relative contributions of electroelastic constants are determined. These results are used to construct ''piezoresponse contrast mechanism maps'' that correlate the imaging conditions with the PFM contrast mechanisms. Conditions for quantitative PFM imaging are set forth. Variable-temperature PFM imaging of domain structures in $BaTiO_3$ and the temperature dependence of the piezoresponse are compared with Ginzburg-Devonshire theory. An approach to the simultaneous acquisition of piezoresponse and surface potential images is proposed.

DOI: 10.1103/PhysRevB.65.125408 PACS number(s): 77.65.−j, 77.80.Bh, 77.80.Dj, 73.30.+y

I. INTRODUCTION

In recent years, scanning probe microscopy (SPM) based techniques have been successfully employed in the characterization of ferroelectric surfaces on the micron and nanometer levels.[1] The primary SPM techniques used are variants of noncontact electrostatic SPM such as electrostatic force microscopy (EFM), scanning surface potential microscopy (SSPM),[2,3] and contact techniques such as piezoresponse force microscopy (PFM).[4–7] Both SSPM and PFM are based on voltage modulation: i.e., during imaging, the actuator driving the cantilever is disengaged and an ac bias is applied directly to a conductive tip. In PFM the tip is in contact with the surface and the electromechanical response of the surface is detected as the first-harmonic component of the bias-induced tip deflection. In SSPM the tip is held at a fixed distance above the surface (typically 10–100 nm) and the first harmonic of the electrostatic force between the tip and surface is nullified by adjusting the constant bias on the tip. An open loop version of SSPM, in which the feedback is disengaged and the oscillation amplitude in the noncontact regime is collected as the image, has also been reported.[8]

In many cases, the morphological information on domain structure and orientation obtained from SPM images is sufficient, and numerous observations of local domain dynamics as related to polarization switching processes,[9–11] ferroelectric fatigue,[12–15] phase transitions,[16–19] mechanical stresses,[20] etc., have been made. However, analysis of local ferroelectric properties including hysteresis measurements,[21] stress effects in thin films,[22] size dependence of ferroelectric properties,[23,24] etc., requires quantitative interpretation of the SPM interaction. A detailed analysis of EFM and SSPM imaging on ferroelectric surfaces is given by Kalinin and Bonnell.[25] Contrast formation mechanism in PFM is less understood.[26–30] Luo *et al.*[17] have found that the temperature dependence of piezoresponse contrast is similar to that of spontaneous polarization. This behavior was attributed to the dominance of electrostatic interactions due to the presence of a polarization bound charge,[31] since the electromechanical response based on the piezoelectric coefficient d_{33} would diverge in the vicinity of the Curie temperature. The presence of the electrostatic forces hypothesis is also supported by observations of nonpiezoelectric surfaces.[32] In contrast, the existence of a lateral PFM signal[33–35] and the absence of relaxation behavior in PFM contrast as opposed to SSPM contrast,[36,25] as well as numerous observations using both EFM-SSPM and PFM,[37,38] clearly point to a significant electromechanical contribution to PFM contrast. In order to resolve the controversy regarding the origins of PFM contrast, we analyze the contrast formation mechanism and relative magnitudes of electrostatic versus electromechanical contributions to PFM interactions for the model case of c^+, c^- domains in tetragonal perovskite ferroelectrics. It is shown that both electrostatic and electromechanical interactions can contribute to the PFM image. The relative contributions of these interactions depend on the experimental conditions. Contrast mechanism maps were constructed to delineate the regions with dominant electrostatic and electromechanical interactions. Under some conditions, i.e., those corresponding to a relatively large indentation force and tip radius, the real piezoelectric coefficient can be determined. This analysis reconciles existing discrepancies in the interpretation of PFM imaging contrast.

II. PRINCIPLES OF PFM

Piezoresponse force microscopy is based on the detection of bias-induced surface deformation. The tip is brought into contact with the surface, and the piezoelectric response of the surface is detected as the first-harmonic component of bias-induced tip deflection $d=d_0+A\cos(\omega t+\varphi)$. The phase φ yields information on the polarization direction below the tip. For c^- domains (polarization vector pointing downward) the application of a positive tip bias results in the expansion of the sample and surface oscillations are in phase with the tip voltage, $\varphi=0$. For c^+ domains, $\varphi=180°$. The amplitude A defines the local electromechanical response and depends on the geometry of the tip-surface system and material properties. An additional contribution to PFM contrast originates from long-range electrostatic tip-surface interactions.[39] This

electrostatic interaction is comprised of a local contribution due to the tip apex and a nonlocal contribution due to the cantilever.[40] Distinguishing electrostatic forces in a PFM experiment is problematic; however, it can be achieved in SSPM. In SSPM, application of an ac bias to the tip located at 10–100 nm from the surface results in a strong capacitive interaction. The cantilever deflection is then proportional to the first harmonic of the force. The amplitude and relative phase of cantilever oscillations in the noncontact mode can be well approximated by simple harmonic-oscillator models.[41]

One of the difficulties in a comparison of the relative magnitudes of electromechanical and electrostatic responses is the difference in the contrast transfer mechanism. In the electromechanical case the surface displacement is determined as a function of applied voltage. In the electrostatic case the force containing both local and nonlocal components is defined. Analysis of contrast formation in PFM clearly requires reliable estimates of surface displacement under tip bias for both cases. Given this, frequency-dependent surface-tip contrast transfer could be constructed.

Analysis of the image formation mechanism requires the solution of several independent problems. The electrostatic tip-surface interaction and the magnitude of electrostatic contrast are analyzed in Sec. III. The mechanism of electromechanical contrast and weak- and strong-indentation limits are formulated in Sec. IV. PFM contrast mechanism maps and the temperature dependence of PFM contrast on a $BaTiO_3$ surface are analyzed in Sec. V.

III. ELECTROSTATIC REGIME

In the electrostatic regime of piezoresponse imaging the capacitive and Coulombic tip-surface interactions result in an attractive force between the tip and surface which cause an indentation. In some cases, these interactions have been approximated by a plane-plane capacitor. Obviously, this is inapplicable in contact because a capacitive force in planar geometry does not cause a tip deflection. A correct description of the electrostatic tip-surface interaction must take into account the tip shape.

A. Potential distribution in the tip-surface junction

The potential distribution in the tip-surface junction in noncontact imaging is often analyzed in the metallization limit for the surface.[42] In this limit, the tip-surface capacitance $C_d(z,\kappa)$, where z is the tip-surface separation and κ is the dielectric constant for the sample, is approximated as $C_d(z,\kappa)\approx C_c(z)$, where $C_c(z)$ is the tip-surface capacitance for a conductive tip and conductive surface. This approximation breaks down for small tip-surface separations when the effect of field penetration in the dielectric sample is nonnegligible. For ferroelectric surfaces the effective dielectric constant is high, $\kappa\approx 100-1000$, favoring the metallization limit. However, in contact tip-surface separation $z\approx 0$ leads to a divergence in the capacitance $C_c(z)$ and the corresponding force. To avoid this difficulty and, more importantly, take into account the anisotropy of the ferroelectric medium, we calculate the tip-surface force using the image charge method for spherical tip geometry. This approach is applicable when the tip-surface separation is small, $z \ll R$, where R is radius of curvature of the tip.

TABLE I. Image charges for conductive, dielectric, and anisotropic dielectric planes.

	Conductive	Isotropic dielectric	Anisotropic dielectric
Q'	$-Q$	$-\frac{\kappa-1}{k+1}Q$	$-\frac{\sqrt{\kappa_z\kappa_x}-1}{\sqrt{\kappa_z\kappa_x}+1}Q$
d'	$-d$	$-d$	$-d$
Q''	0	$\frac{2\kappa}{k+1}Q$	$\frac{2\sqrt{\kappa_z\kappa_x}}{\sqrt{\kappa_z\kappa_x}+1}Q$
d''		d	$d\sqrt{\kappa_z/\kappa_x}$

The potential in air produced by charge Q at a distance d above a conductive or dielectric plane located at $z=0$ can be represented as a superposition of potentials produced by the original charge and the corresponding image charge Q' located at position $z=d'$ below the plane. The potential in a dielectric material is equal to that produced by a different image charge Q'' located at $z=d''$.[43,44] Values of Q', Q'', d', and d'' for metal and isotropic or anisotropic dielectric materials are summarized in Table I. Note that the potential in air above an anisotropic dielectric material is similar to the isotropic case with an effective dielectric constant $\kappa_{\text{eff}}=\sqrt{\kappa_x\kappa_z}$, where κ_x and κ_z are the principal values of the dielectric constant tensor. Potential and field distributions inside the dielectric material are more complex[45] and are out of the scope of the present paper.

To address tip-surface interactions and taking the effect of the dielectric medium into account, the image charge distribution in the tip can be represented by charges Q_i located at distances r_i from the center of the sphere such that

$$Q_{i+1}=\frac{\kappa-1}{\kappa+1}\frac{R}{2(R+d)-r_i}Q_i, \tag{1a}$$

$$r_{i+1}=\frac{R^2}{2(R+d)-r_i}, \tag{1b}$$

where R is tip radius, d is tip-surface separation, $Q_0=4\pi\varepsilon_0 RV$, $r_0=0$, and V is the tip bias. The tip-surface capacitance is

$$C_d(d,\kappa)=\frac{1}{V}\sum_{i=0}^{\infty}Q_i, \tag{2}$$

from which the force can be found. The rotationally invariant potential distribution in air can be found from Eqs. (1a) and (1b). Specifically, the potential on the surface directly below the tip is

$$V(0,0)=\frac{1}{4\pi\varepsilon_0}\frac{2}{\kappa+1}\sum_{i=0}^{\infty}\frac{Q_i}{R+d-r_i}. \tag{3}$$

In the conductive surface limit, $\kappa=\infty$ and Eq. (2) is simplified to[46]

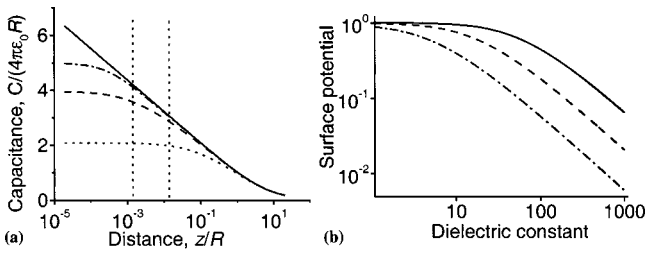

FIG. 1. (a) Tip-dielectric surface capacitance for $\kappa=10$ (dotted line), $\kappa=100$ (dashed line), and $\kappa=1000$ (dot-dashed line), compared to the metallic limit (solid line). Vertical lines delineate the region of characteristic tip-surface separations (0.1–1 nm) in contact mode for tip radius $R=50$ nm. (b) Surface potential below the tip for tip-surface separations $z=0.1\ R$ (dot-dashed line), $z=0.01\ R$ (dashed line), and $z=0.001\ R$ (solid line) as a function of the dielectric constant of the surface.

$$C_c = 4\pi\varepsilon_0 R \sinh\beta_0 \sum_{n=1} (\sinh n\beta_0)^{-1}, \tag{4}$$

where $\beta_0 = \operatorname{arccosh}[(R+d)/R]$. For the conductive tip-dielectric surface,

$$C_d = 4\pi\varepsilon_0 R \sinh\beta_0 \sum_{n=1} \left(\frac{\kappa-1}{\kappa+1}\right)^{n-1} (\sinh n\beta_0)^{-1}. \tag{5}$$

While in the limit of small tip-surface separation C_c diverges logarithmically, C_d converges to the universal ''dielectric'' limit[47]

$$C_d(\kappa)_{z=0} = 4\pi\varepsilon_0 R \frac{\kappa-1}{\kappa+1} \ln\left(\frac{\kappa+1}{2}\right). \tag{6}$$

The distance dependence of the tip-surface capacitance and surface potential directly below the tip are shown in Figs. 1(a) and 1(b). For relatively large tip-surface separations, $C_d(z,\kappa)\approx C_c(z)$, which is the usual assumption in noncontact SPM imaging. The most prominent feature of this solution is that, while for low-κ dielectric materials the tip-surface capacitance achieves the dielectric limit in contact and hence surface potential is equal to the tip potential, this is not the case for high-κ materials. The tip-surface capacitance, capacitive force, and electric field can be significantly smaller than in the dielectric limit. The surface potential below the tip is smaller than the tip potential and is inversely proportional to dielectric constant [Fig. 1(b)]. This is equivalent to the presence of an apparent dielectric gap between the tip and surface that attenuates the potential, which is often the explanation for experimental observations.

B. Tip-surface interaction in the electrostatic regime

From Eqs. (2), (4), and (5), the magnitudes of capacitive and Coulombic forces between the cantilever-tip assembly and the surface can be estimated. The capacitive force is

$$2F_{\rm cap} = C'_{\rm loc}(V_{\rm tip}-V_{\rm loc})^2 + C'_{\rm nl}(V_{\rm tip}-V_s)^2, \tag{7}$$

where $V_{\rm tip}$ is the tip potential, $V_{\rm loc}$ is the domain-related local potential directly below the tip, V_s is the surface potential averaged over the distance comparable to the cantilever length, $C'_{\rm loc}$ is the local part of tip-surface capacitance gradient, and $C'_{\rm nl}$ is the nonlocal part due to the cantilever. Typically, the cantilever length is significantly larger than the characteristic size of ferroelectric domains; therefore, the nonlocal part results in a constant background on the image that does not preclude qualitative domain imaging. The nonlocal capacitance gradient can be estimated using plane-plane geometry as $C'_{\rm nl}=\varepsilon_0 S(z+L)^{-2}$, where S is the effective cantilever area and L is the tip length. For a typical tip with $L\approx 10\ \mu$m and $S\approx 2\times 10^3\ \mu$m^2, the nonlocal contribution is $C'_{\rm nl}\approx 1.8\times 10^{-10}$ F/m and is independent of the tip radius. The force for a tip-surface potential difference of 1 V is $F_{\rm nl}\approx 0.9\times 10^{-10}$ N. (The nonlocal contribution rigorously should also contain a term describing an effect of the conical part of the tip.[25]) The local capacitive contribution due to the tip apex is $F_{\rm loc}=1.4\times 10^{-8}$ N for $z=0.1$ nm, $R=50$ nm, i.e., two orders of magnitude larger. However, $C'_{\rm loc}$ scales linearly with tip radius and, therefore, for the sharp tips capable of high-resolution nonlocal contributions to the signal increase. Similar behavior is found for noncontact SPMs.[48] The Coulombic tip-surface interaction due to the polarization charge can be estimated using the expression for the electric field above a partially screened ferroelectric surface, $E^u=(1-\alpha)P\varepsilon_0^{-1}(1+\sqrt{\kappa_x\kappa_z})^{-1}$, where α is the degree of screening and P is spontaneous polarization ($P=0.26$ C/m^2 for $BaTiO_3$). For unscreened surfaces, $\alpha=0$, so this Coulombic contribution in the limit $F_{\rm Coul}\ll F_{\rm cap}$ is $F_{\rm Coul}=C_{\rm loc}(V_{\rm tip}-V_{\rm loc})E^u$ and for the same tip parameters as above $F_{\rm Coul}=2.2\times 10^{-9}$ N. However, polarization charge is almost completely screened in air, typically $1-\alpha\ll 10^{-3}$, and under these conditions the Coulombic contribution can be excluded from the electrostatic tip-surface interaction.

Capacitive force results in an indentation of the surface. In the Hertzian approximation the relationship between the indentation depth h, tip radius of curvature R, and load P is[49]

$$h = \left(\frac{3P}{4E^*}\right)^{2/3} R^{-1/3}, \tag{8}$$

where E^* is the effective Young's modulus of the tip-surface system defined as

$$\frac{1}{E^*} = \frac{1-\nu_1^2}{E_1} + \frac{1-\nu_2^2}{E_2}. \tag{9}$$

E_1, E_2 and ν_1, ν_2 are Young's moduli and Poisson ratios of tip and surface materials (Fig. 2). For ferroelectric perovskites Young's modulus is of the order of $E^*\approx 100$ GPa. The contact radius a is related to the indentation depth as $a=\sqrt{hR}$. Hertzian contact does not account for adhesion, and capillary forces in a tip-surface junction and a number of more complex models for nanoindentation processes are known.[50]

Under typical PFM operating conditions the total force acting on the tip is $F=F_0+F_{\rm el}$, where $F_0=k\ d_0$ is the elastic force exerted by the cantilever of the spring constant k at set point deflection d_0 and $F_{\rm el}$ is the electrostatic force. Since

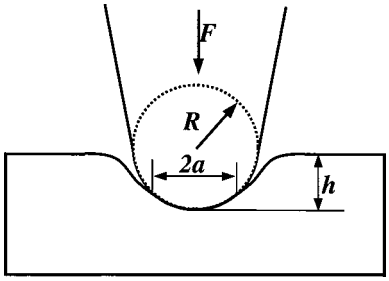

FIG. 2. Geometry of the tip indenting the piezoelectric surface.

the electrostatic force is modulated, $V_{tip}=V_{dc}+V_{ac}\cos(\omega t)$, the first harmonic of tip deflection is

$$h_{1\omega}=\frac{\chi}{2\pi\omega}\int [F_0+C'_{loc}(V_{dc}+V_{ac}\cos(\omega t) - V_{loc})^2]^{2/3}\cos(\omega t)dt, \quad (10)$$

where $\chi=(3/4E^*)^{2/3}R^{1/3}$. In the limit when the indentation force is much larger than electrostatic force, $F_{el}\ll F_0$, the effective spring constant of the tip-surface junction is $k_{eff}=\partial P/\partial h$ and the first harmonic of the cantilever response is $h_{1\omega}=F_{1\omega}/k_{eff}$. For a Hertzian indentation the response is

$$h_{1\omega}=\frac{2}{3}\left(\frac{3}{4E^*}\right)^{2/3}R^{-1/3}F_0^{-1/3}F_{1\omega}. \quad (11)$$

This equation can be also obtained directly from an expansion of the integrand in Eq. (10). For typical PFM imaging conditions the set point deflection is ~100 nm and the spring constant of the cantilever k varies from ~0.01 to ~100 N/m. Consequently, imaging can be done under a range of loads spanning at least 4 orders of magnitude from 1 nN to 10 μN. For $F_0=100$ nN, $E^*=10^{11}$ Pa, and the potential difference between the domains $\Delta V=150$ mV, the PFM contrast between the domains of opposite polarities is $\Delta h_{1\omega}=6.02\times10^{-12}$ m/V. It should be noted that the potential difference between ferroelectric domains in the ambient is determined by the properties of the adsorbate layer that screens spontaneous polarization.[51] Under UHV conditions where the intrinsic screening by charge carriers[52] dominates the potential difference would be larger and can achieve the limiting value of $\Delta V=3$ V comparable to the band gap. In this case, the electrostatic PFM contrast between the domains of opposite polarities can be as large as $\Delta h_{1\omega}=1.2\times10^{-10}$ m/V.

It is useful to consider the effect of cantilever stiffness on the electrostatic contrast. For soft cantilevers the indentation depth can be extremely small. The electrostatic tip-surface and even cantilever-surface interaction can dominate over the elastic load, especially for the large potential difference between the tip and surface typical during hysteresis measurements or polarization switching. In this case, the linear approximation of Eq. (11) is no longer valid. In the small signal approximation $V_{ac}\to0$, the response amplitude can still be obtained from Eq. (10) where the effective load is now $F_0=kd_0+C'_{loc}(V_{dc}-V_{loc})^2$, predicting a decrease of response with bias. Interestingly enough, the integral in Eq. (10) is nullified for zero tip-surface potential difference, $V_{dc}-V_{loc}=0$. Therefore, the imaging mechanism bears a close similarity to that of noncontact open-loop SSPM and feedback can be employed to obtain a nulling potential map on any surface. On piezoelectric surfaces the electromechanical contribution is nonzero and the nulling condition does not correspond to the equilibrium surface potential. For a small indentation force the cantilever dynamics is expected to be significantly more complex; the tip can lose contact with the surface in the upper part of the trajectory, the cantilever vibration can be significant, etc.

The crossover from the linear response, Eq. (11), to the nonlinear behavior for driving voltages of $V_{ac}=2$ V is expected for spring constants $k\approx1$ N/m, defining the generic difference between ''soft'' and ''stiff'' cantilevers.

IV. ELECTROMECHANICAL REGIME

The electrostatic regime considered above can be applied to any dielectric surface; however, for ferroelectric and, more generally, piezoelectric materials, an additional bias-induced effect is a linear electromechanical response of the surface. A rigorous mathematical description of the problem is extremely complex; fortunately, the geometry of the tip-surface junction in PFM is remarkably similar to the piezoelectric indentation problem.[53–57] In the classical limit, the coupled electromechanical problem is solved for mixed-value boundary conditions: $V_s=V_{tip}$ in the contact area and the normal component of the electric field $E_z=0$ elsewhere. However, in the typical PFM experiment the contact area is small and deformation occurs even when the tip is not in contact due to the local electric field. In this case, the zero-field approximation outside of the contact area is invalid; instead, the contact area itself can be neglected and the surface deformation can be ascribed solely to field effects. Therefore, we distinguish two limits for the PFM electromechanical regime.

(i) Strong (classical) indentation: $V=V_{tip}$ in the contact area, $E_z=0$ elsewhere.

(ii) Weak (field-induced) indentation: contact area is negligible, $E_z\neq0$.

In practice, both mechanisms might operate and the dominant contribution depends on the imaging parameters.

A. Strong indentation

A complete description of the strong-indentation limit is given by Giannakopoulos and Suresh,[55] who extended Hertzian contact mechanics to piezoelectric materials. The relationship between the load P, indentor potential V, and indentation depths h is

$$h=\frac{a^2}{R}+\frac{2\beta}{3\alpha}V, \quad (12a)$$

$$P=\alpha\frac{a^3}{R}-\beta aV, \quad (12b)$$

where α and β are material-dependent constants and a is the contact radius. Solving Eqs. (12a) and (12b) for indentation depth as a function of indentor bias relevant for PFM yields

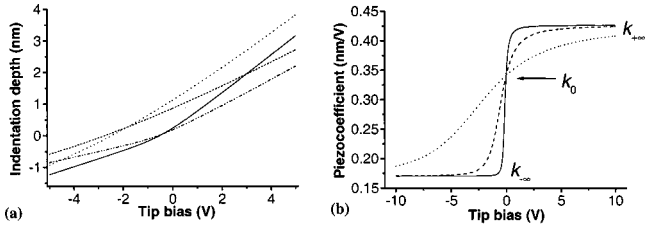

FIG. 3. Indentation depth as a function of tip bias for different compositions and loads in the strong-indentation limit (a) and piezoresponse coefficient of $BaTiO_3$ as a function of tip bias for different loads (b).

a surface deformation as illustrated in Fig. 3(a). For small modulation amplitudes, the PFM contrast is $h_{1\omega} \approx h'(F,V_{dc})V_{ac}$, where the functional form of $h(F,V_{dc})$ is given by Eqs. (12a) and (12b). The bias dependence of the piezoresponse coefficient is given by the local slope, $k = h'(F,V_{dc})$, shown in Fig. 3(b). For $V_{dc}=0$ the asymptotic analysis of Eqs. (12a) and (12b) for the c^+ orientation yields $k_0=\frac{4}{3}\beta/\alpha$, while for $V_{dc}\to+\infty$ and $V_{dc}\to-\infty$ the respective limits are $k_{+\infty}=\frac{5}{3}\beta/\alpha$ and $k_{-\infty}=\frac{2}{3}\beta/\alpha$ [Fig. 3(b)] and are independent of the tip radius and contact force. The response amplitude in the strong-indentation limit is high and comparable to the corresponding d_{33} value (Table II).

The applicability of the strong-indentation regime to PFM contrast is limited. A high dielectric constant leads to a significant potential drop between the tip and surface, $V_s \ll V_{tip}$; therefore, for an infinitely stiff tip and surface, the basic assumption of the strong-indentation limit, $V_s=V_{tip}$ in the contact area, is not fulfilled. Even for finite contact the potential on the surface below the tip is lower than the tip potential and differs from that assumed in the strong indentation limit. It is useful to consider the effect of contact radius on this assertion. A simple approximation for the surface potential below the tip is $V_s=\gamma V_{tip}$ in the contact area, where γ is the attenuation factor [Figs. 4(a) and 4(b)]. Such behavior is referred to as contact-limited strong indentation (CSI). Using a spherical approximation for the contact region, the attenuation factor is estimated as $\gamma=(1+w\kappa_{eff}/a\kappa_d)^{-1}$, where w is the thickness of the "apparent" dielectric gap ($w\geqslant 0.1$ nm), κ_d is the dielectric constant in the gap ($\kappa_d=1-100$), a is the contact radius, and κ_{eff} is the effective dielectric constant of the ferroelectric material. For planar geometry (i.e., $R\gg a\gg w$), κ_{eff} is close to κ_z for a ferroelectric material. For the spherical case, κ_{eff} is close to $\sqrt{\kappa_x\kappa_z}$, imposing an upper and lower limit on κ_{eff}. For a metallic tip the gap effect is expected to be minimal,

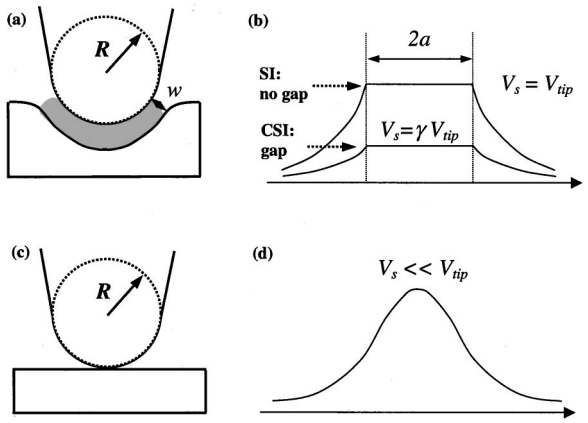

FIG. 4. Tip-surface junction (a) and surface potential (b) in the strong-indentation limit with and without the apparent gap effect and tip-surface junction (c) and surface potential (d) in the weak-indentation limit.

while for doped silicon tips w will be comparable to the depletion width of the tip material. Even for thin dielectric layers (0.1–1 nm) the effective surface potential can be attenuated by as much as a factor of 100 due to a large difference between the dielectric constants of dielectric and ferroelectric materials. For imperfect contact the magnitude of the piezoresponse in the strong-indentation limit can become comparable to that of the electrostatic mechanism. The deviation of the tip shape from spherical (e.g., flattening due to wear, etc.) reduces the electrostatic response due to a higher contact stiffness and increases the electromechanical response. The resolution in the strong-indentation limit is limited by the indentation radius a.

B. Weak indentation

Weak indentation presents the other limiting case in the PFM experiment when the indentation load and contact area are small. In this limit, the contribution of the contact area to the total electromechanical response of the surface can be neglected (Figs. 4(c) and 4(d)). The potential distribution in the tip-surface junction is calculated in the rigid electrostatic limit as shown in Sec. III A, provided that the dielectric constant of the material is sufficiently high. The electromechanical response of the surface is calculated using the Green's function for point force and charge obtained by Karapetian *et al.*:[57]

$$h(r)=f\frac{A}{r}+q\frac{L(s_{ij},e_{ij},\varepsilon_{xx},\varepsilon_{zz})}{r}, \tag{13}$$

TABLE II. Piezoresponse constants for different materials.

Composition	Bulk d_{33} (m/V)	α (N/m^2)	β (N/mV)	Strong indentation k_0 (m/V)	Weak indentation L (m^2/C)	Weak indentation d_{eff} (m/V)
$BaTiO_3$	1.9×10^{-10}	1.76×10^{11}	44.9	3.40×10^{-10}	1.54×10^{-3}	1.10×10^{-10}
PZT4	2.91×10^{-10}	1.18×10^{11}	43.9	4.96×10^{-10}	2.41×10^{-3}	1.71×10^{-10}
PZT5a	3.73×10^{-10}	9.98×10^{10}	45.2	6.04×10^{-10}	2.66×10^{-3}	2.05×10^{-10}

where h is the vertical displacement, r is the radial coordinate, f is the point force, q is the point charge, A and L are material-dependent constants, and r is the distance from the indentation point. For a distributed charge, the surface deformation is

$$h(\mathbf{r}) = L \int \frac{\sigma(\mathbf{r}_0)}{|\mathbf{r}-\mathbf{r}_0|}\,\mathrm{dS}, \tag{14}$$

where

$$\sigma(\mathbf{r}_0) = \varepsilon_0 E_z(\mathbf{r}_0).$$

The materials properties affect the PFM contrast through the coefficient L, while the geometric properties are described by the (material-independent) integral.

For spherical tip geometry, the electromechanical surface response in the weak-indentation limit can be evaluated using the image charge method developed in Sec. III A. The surface charge density induced by point charge Q at distance l from a conductive or high-κ dielectric surface is

$$\sigma_0 = \frac{Q}{4\pi} \frac{2d}{(l^2+r^2)^{3/2}}.$$

From Eq. (14), the charge-induced piezoelectric deformation of the surface is $h = QL/l$. Using the same image charge series developed in Sec. III A, total tip-induced surface deformation is

$$h = L\sum_{i=0}^{\infty} \frac{Q_i}{R+d-r_i} = LG(R,d). \tag{15}$$

Note that this expression is remarkably similar to that of the tip-induced surface potential [Eq. (3)]. Thus the piezoresponse in the weak-indentation limit can be related to the tip-induced surface potential V_s as $h = 2\pi\varepsilon_0 L(\kappa+1)V_s$. Specifically, the surface deformation is linear in the surface potential, $h = d_{\mathrm{eff}} V_s$, where the effective piezoresponse constant d_{eff} in the weak-indentation limit is $d_{\mathrm{eff}} = 2\pi\varepsilon_0 L(\sqrt{\kappa_x\kappa_z}+1)$.

For $R = 50$ nm, $d = 0.1$ nm, and a typical value of $L \approx 2.5\times10^{-3}$ m^2/C the characteristic piezoresponse amplitude in the weak-indentation limit is $h \approx 6.54\times10^{-12}$ m/V. The distance and tip radius dependence of the response is $h \sim (R/d)^{0.5}$, in agreement with a previously used point charge approximation.[58] The effective piezoelectric constant d_{eff} for the weak-indentation limit is remarkably similar to k_0 for the strong-indentation limit as shown in Table II. The difference between the limits arises from the disparate ways the dielectric gap is taken into account (Fig. 4). The weak-indentation limit accounts for the effect of the gap directly in the functional form of coefficient L, which incorporates the dielectric properties of the surface [Fig. 4(c)]. In the strong-indentation limit, the effective dielectric gap must be introduced through the attenuation factor γ. The resolution in the weak-indentation limit is determined by the tip radius of curvature and effective tip-surface separation and is proportional to $\sqrt{Rh}$.

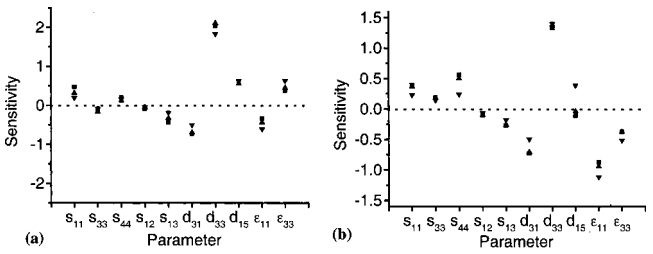

FIG. 5. Sensitivity in the strong- (a) and weak- (b) indentation limits in the $(s_{ij}, d_{ij}, \varepsilon_{ij})$ representation for $BaTiO_3$ (■), PZT4 (▲), and PZT5a (▼).

C. Effect of materials properties on the response

A complete analysis of the electromechanical response of the surface in terms of materials properties is difficult. Even in the ideal case of known geometry, both strong- and weak-indentation limits lead to complex expressions that include ten electroelastic constants for a transversally isotropic medium. In order to clarify the relative contributions of different electroelastic constants to PFM, responses both in the strong- and weak-indentation limits are calculated for a variety of ferroelectric materials.[59–61] A sensitivity function of the piezoresponse (PR) is defined as

$$S(f_{ij}) = [\mathrm{PR}(f_{ij} = 1.1f_{ij}^0) - \mathrm{PR}(f_{ij} = 0.9f_{ij}^0)]/[0.2\mathrm{PR}(f_{ij} = f_{ij}^0)], \tag{16}$$

where f_{ij} is a selected electroelastic constant and f_{ij}^0 is a reference value for that constant. A positive value of $S(f_{ij})$ implies that a higher constant favors the piezoresponse, while a negative value of $S(f_{ij})$ suggests that the response decreases with this constant. $S(f_{ij}) \approx 0$ indicates that the response is independent of that property. The sensitivity of the piezoresponse for several ferroelectric materials is shown in Fig. 5. The piezoresponse in the strong-indentation limit is clearly dominated by the d_{33} of the material, while other electroelastic constants provide minor contributions [Fig. 5(a)]. In the weak-indentation limit both d_{33} and ε_{11} strongly influence the response, significant contributions being provided by d_{31} and ε_{33} as well [Fig. 5(b)]. The response increases with d_{33} and decreases with ε_{11} as expected. The response in both limits does not depend on the elastic stiffness c_{12} [Figs. 5(a) and 5(b)]. Similar diagrams can be constructed for sensitivity as a function of elastic compliances s_{ij} and piezoelectric constants e_{ij}; however, in this representation the contributions of all constants are comparable.

The goal is to determine under what conditions a correlation exists between the measured piezoresponse and d_{33} of the material. Most early treatments of piezoresponse image contrast explicitly assumed that the response is proportional or equal to d_{33}. To test this assertion, the calculated piezoresponse coefficient is compared to the piezoelectric constant for a series of ferroelectric materials. An almost linear correlation exists between the response in the strong-indentation limit and d_{33}, $\mathrm{PR} \sim 1.5d_{33}$ [Fig. 6(a)]. In contrast, no such correlation is observed between L and d_{33} for the weak-indentation limit [Fig. 6(b)]. The physical origin of this behavior is that L defines the response of the surface to charge

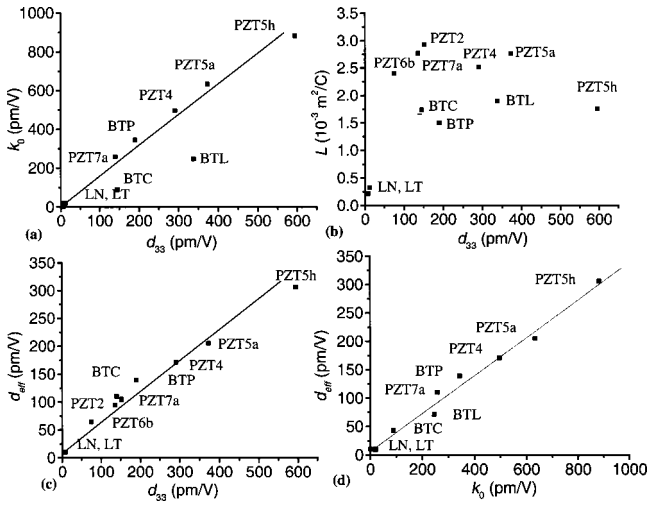

FIG. 6. Correlation between piezoresponse and d_{33} in the strong- (a) and weak- (b) indentation limits for some polycrystal and single-crystal materials. The correlation between effective piezoelectric constants d_{eff} and d_{33} in the weak-indentation limit (c) and correlation between d_{eff} and the piezoresponse in the strong-indentation limit (d). PZT denotes different types of commercial lead zirconate-titanate ceramics, LN and LT are $LiNbO_3$ and $LiTiO_3$, BTC is 95% $BaTiO_3$/5% $CaTiO_3$ (ceramic *B*), and BTP and BTL are $BaTiO_3$ polycrystals.

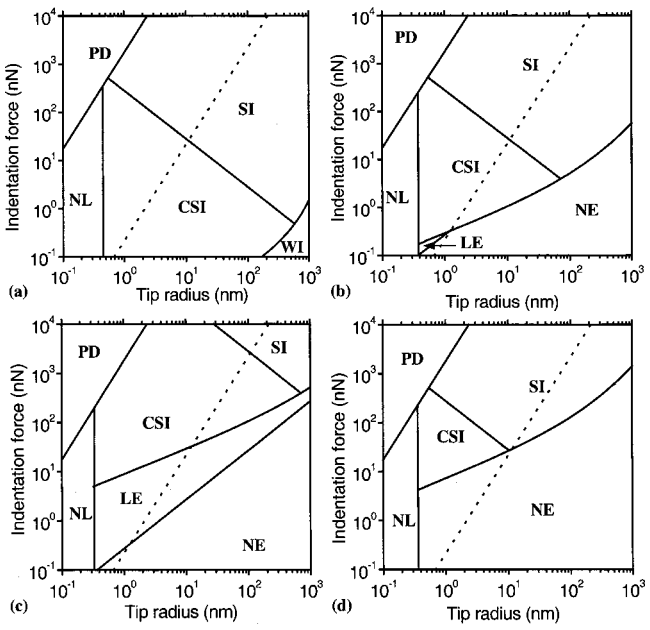

FIG. 7. Contrast mechanism maps of piezoresponse force microscopy. SI is the strong-indentation regime, CSI the contact-limited strong indentation regime, WI the weak-indentation regime, LE the linear electrostatic regime, NE the nonlinear electrostatic regime, NL the nonlocal interactions, and PD the plastic deformation. The dotted line delineates the region where stress-induced switching is possible. (a) $w=0.1$ nm, $\Delta V=V_{\mathrm{tip}}$-$V_s=0$ V, (b) $w=0.1$ nm, $\Delta V=1$ V, (c) $w=1$ nm, $\Delta V=1$ V, and (d) $w=0.1$ nm, $\Delta V=5$ V.

and therefore depends on ratios of the type d_{ij}/ε_{ij}. According to the Ginzburg-Devonshire theory, these ratios are proportional to the corresponding second-order electrostriction coefficients, $d_{ij}/\varepsilon_{ij}\sim Q_{ij}P$. Therefore, the effects of the electromechanical coupling coefficient and dielectric constants counteract each other. On the other hand, the effective piezoelectric constant in the weak-indentation limit, d_{eff}, exhibits a good correlation with d_{33}, $d_{\mathrm{eff}}\sim 0.5 d_{33}$ [Fig. 6(c)]. The effective piezoelectric response constants in the weak- and strong-indentation limits exhibit an almost perfect linear dependence, $d_{\mathrm{eff}}=0.33k_0$ [Fig. 6(d)]. Despite this similarity, the strong-indentation limit describes the surface deflection induced by a known *potential* in the contact area, while the weak-indentation limit yields the surface deflection due to a known tip-induced *charge distribution* on the surface.

V. EFFECT OF THE IMAGING CONDITIONS

In the PFM measurement the contrast mechanism will depend on details of the experimental conditions. Depending on the tip radius and indentation force, both linear and nonlinear electrostatic interactions and strong- and weak-indentation regimes can occur. In order to relate PFM imaging mechanisms to experimental conditions, contrast mechanism maps were constructed as shown in Fig. 7. To delineate the regions with dominant interactions, surface deformation in the electrostatic case was estimated using the distance dependence of the tip-surface capacitance as $F_{1\omega}=2.7\times 10^{-8}(R/50)(0.1/d)(V_{\mathrm{tip}}-V_s)V_{\mathrm{ac}}N$, where both R and d are in nanometers. The surface deformation $h_{1\omega}^{\mathrm{el}}$ was calculated from Eq. (11). The boundaries of the nonlocal regions are established by a comparison of tip apex-surface capacitance and cantilever-surface capacitance.[62] Surface deformation in the electromechanical regime was calculated including the ''apparent dielectric gap'' effect as $h_{1\omega}^{\mathrm{em}}=d_{\mathrm{eff}}/(1+w\kappa_{\mathrm{eff}}/a\kappa_d)$, where the contact radius a is given by the Hertzian model and $\kappa_{\mathrm{eff}}/\kappa_d=30$. The boundary between the strong- and weak-indentation regimes is given by an attenuation factor of 0.3. The boundary between the electromechanical and electrostatic regions is given by the condition $h_{1\omega}^{\mathrm{em}}=h_{1\omega}^{\mathrm{el}}$. For small indentation forces a nonlinear dynamic behavior of the cantilever is expected and the corresponding condition is $F_{\mathrm{el}}=F_0$. For very large indentation forces, the load in the contact area can be sufficient to induce plastic deformation of the surface or tip. The onset of this behavior is expected when $F_0/\pi a^2=E^*$. High pressures in the contact area can significantly affect the ferroelectric properties of the material and induce local polarization switching, etc.,[63–65] at a strain $P/d_{33}\sim 3\times 10^9$ N/m^2 for a typical ferroelectric material. The effect of the tip-surface potential difference and driving amplitude on imaging can be analyzed using formalism presented in Secs. III and IV.

The contrast mechanism map in Fig. 7(b) corresponds to imaging under good tip-surface contact ($w=0.1$ nm) and zero tip-surface potential difference. The crossover from contact-limited strong indentation to the strong-indentation limit depends on the choice of the attenuation factor. Pure weak-indentation behavior is observable only for large tip

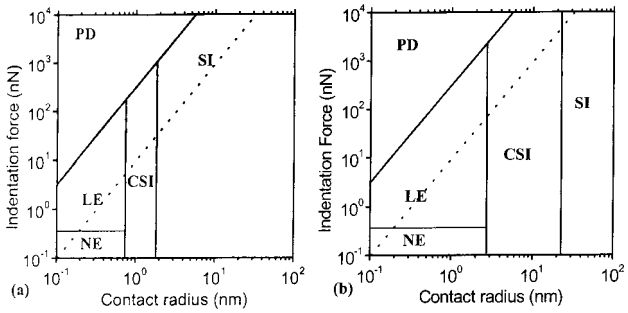

FIG. 8. Contrast mechanism maps of piezoresponse force microscopy as a function of contact radius and indentation force. SI corresponds to the strong-indentation regime, CSI the contact-limited strong indentation regime, WI the weak-indentation regime, LE the linear electrostatic regime, NE the nonlinear electrostatic regime, and PD the plastic deformation. The dotted line delineates the region where stress-induced switching is possible. The maps are constructed for good tip-surface contact ($w=0.1$ nm) and bad contact ($w=1$ nm).

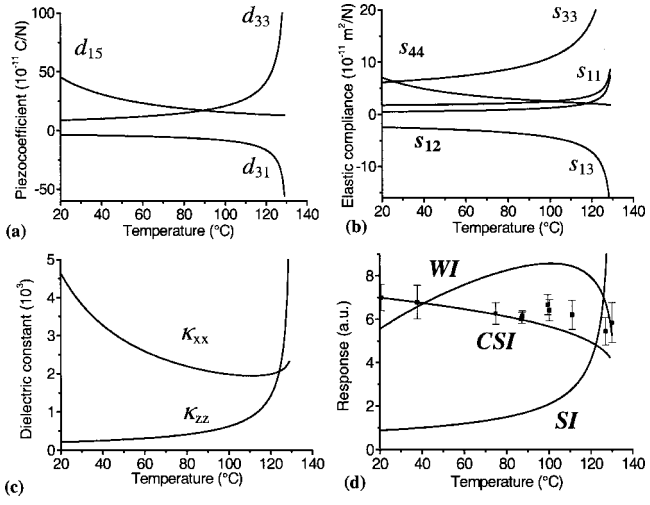

FIG. 9. Temperature dependence of elastic constants (a), piezoelectric constants (b), and dielectric constants (c) for $BaTiO_3$ calculated from Ginzburg-Devonshire theory and temperature dependence of the piezoresponse coefficient in the WI and CSI limits (d). Note that L depends on the ten electroelastic constants of the material. Unlike d_{33}, the response in the weak-indentation and contact-limited strong-indentation regimes does not diverge at the Curie temperature, thus suggesting that PFM contrast on $BaTiO_3$ surfaces is strongly influenced by the dielectric gap effect.

radii and small indentation forces. Typically, the ferroelectric domains are associated with surface potential variations and the tip potential is not equal to the surface potential. The contrast mechanism map in Fig. 7(b) corresponds to imaging under good tip-surface contact ($w=0.1$ nm) and moderate tip-surface potential difference ($V_{\mathrm{tip}}-V_{\mathrm{loc}}=1$ V). Less perfect contact that results from oxidized tips or poorly conductive coating, as well as the presence of contaminants, will expand the weak-indentation and linear electrostatic regions, primarily at the expense of the strong-indentation region [compare Figs. 7(b) and 7(c)]. Increasing the tip-surface potential difference increases the electrostatic contribution [Fig. 7(d)]. Consequently, the nonlinear electrostatic region expands and can even eliminate the linear electrostatic region. However, above a certain tip-surface potential difference or driving voltage the linear approximation, Eq. (11), is no longer valid and Eq. (10) must be used. The effect of high driving voltages and tip-surface potential difference is an increase of the indentation force $F=F_0+C'_{\mathrm{loc}}(V_{\mathrm{tip}}-V_{\mathrm{loc}})^2$, expanding the electromechanical region. If ''true'' PFM is the ability to quantify the piezoelectric coefficient directly from the measurements, it can be achieved only in the strong-indentation region. As shown in Fig. 6, k_0 correlates linearly with d_{33} in the strong-indentation regime. In the weak-indentation regime and contact-limited strong-indentation regime, the properties of the surface can still be obtained indirectly as discussed in Sec. IV B. Finally, in the electrostatic regime the PFM image is dominated by long-range electrostatic interactions and piezoelectric properties of the material are inaccessible. In certain cases the surface charge distribution is directly correlated with ferroelectric domain structure; therefore, qualitative information on domain topology can still be obtained. These results allow multiple controversies in the interpretation of PFM contrast to be reconciled by elucidating experimental conditions under which electrostatic versus electromechanical mechanisms dominate. Acquisition of quantitative information requires blunt tips and intermediate indentation forces to avoid pressure-induced polarization switching: i.e., operation regimes to the right of the dotted line in Fig. 7. The use of a top metallic electrode as proposed by Christman *et al.*[66] is the limiting case of this consideration.

The contrast mechanism maps in Fig. 7 are quantitative for a spherical tip; however, gradual tip wear during the imaging is inevitable and can be easily detected using appropriate calibration standards. The influence of tip flattening on PFM contrast mechanisms is shown in Figs. 8(a) and 8(b). The response was calculated as a function of contact radius for fixed electrostatic force corresponding to $R=100$ nm. In contrast to the spherical case, the contact stiffness for a flat indentor does not depend on the indentation force; hence, the crossover from the electrostatic to electromechanical regime occurs at some critical contact radius. Since the sphere-plane model is less accurate for this case, the degree of approximation associated with it results in the more qualitative nature of the contrast map. It should be noted, however, that the electrostatic force can be measured directly[67] and used for the construction of the map for an individual tip.

The application of these analytical solutions to the temperature dependence of the piezoresponse of $BaTiO_3$ is illustrated in Fig. 9. In the strong-indentation regime, the response is proportional to d_{33} and is expected to diverge with temperature near T_c. The experimental observations do not support this conjecture. The temperature dependence of PFM contrast is calculated according to Karapetian *et al.*[57] for the weak-indentation limit. The temperature dependence of the electroelastic constants for $BaTiO_3$ was calculated by Ginzburg-Devonshire theory[68,69] and the temperature dependence for $L(T)$ is compared to experimental measurements in Fig. 9. The temperature dependence of the piezoresponse

in the contact-limited strong indentation limit is also shown.[19] In contrast to the strong-indentation limit no divergence occurs in the temperature dependence of the weak-indentation and contact-limited strong-indentation limits, consistent with experimental behavior. The physical origin of this behavior is that not only the piezoelectric constant, but also the dielectric constant increases with temperature. Similar behavior has been observed by other authors.[36] Thus the temperature dependence of experimental PFM contrast suggests that under experimental conditions ($F_0 \approx 200$ nN, nominal tip radius $R \approx 30$ nm, tip is not blunted) the imaging mechanism of PFM is governed by the dielectric gap effect. Furthermore, from Fig. 7 the width of the ''apparent gap'' in these measurements can be estimated as >1 nm. This conclusion is verified by small experimental piezoresponse coefficients ($\sim$4 pm/V) (Refs. 70–72) as compared to the calculated value for $BaTiO_3$ ($\sim$50–100 pm/V).

Electrostatic tip-surface interactions can be significantly affected by local surface charging.[73–77] Clearly, elucidating the charge effects in the PFM requires a reliable way to probe the local piezoresponse and long-range electrostatic forces simultaneously. This is especially important for investigations of dynamic phenomena in which large time intervals between sequential PFM-SSPM images are unacceptable. Under equilibrium conditions, simultaneous acquisition of piezoresponse and potential images can facilitate the correlation between topographic, potential, and piezoresponse features and analysis of surface properties. We have shown that simultaneous PFM and SSPM imaging can be implemented using the usual interleave mode so that the topography and piezoresponse are acquired in contact and the potential is collected on the interleave line.[78] Figure 10 illustrates several examples of simultaneous piezoresponse and potential imaging on $BaTiO_3$ and PZT. An open loop version of SSPM is used. For $BaTiO_3$ both SSPM and PFM features are related to the surface domain structure and therefore are closely correlated. For PZT the information provided by the two is complementary. However, after polarization switching the regions with deposited charge and reversed polarization are distinguished. This illustrates the approach to independently obtain information that allows capacitive versus electromechanical interactions to be quantified.

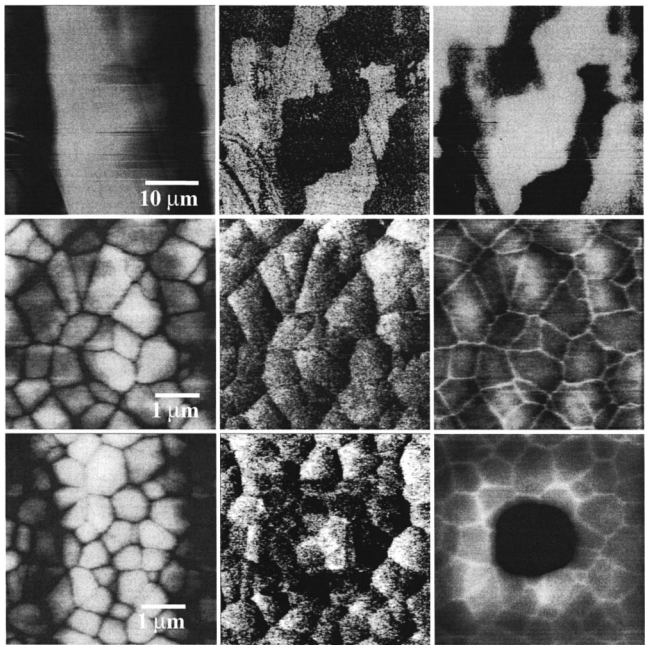

FIG. 10. Surface topography (left), piezoresponse (central), and open loop SSPM (right) images from $a-c$ domains on the $BaTiO_3$ (100) surface (top), for a pristine PZT surface (middle), and for PZT after switching by 10 V at 2.5 μm and -10 V at 1 μm. Potential and piezoresponse images are obtained simultaneously.

VI. SUMMARY

Analytical models for electrostatic and electromechanical contrast in PFM have been developed. Image charge calculations are used to determine potential and field distributions in the tip-surface junction between a spherical tip and an anisotropic dielectric half plane. For high-dielectric-constant materials the surface potential directly below the tip is significantly smaller than the tip potential, implying the presence of an effective dielectric gap. The effect of the unscreened polarization charge during PFM is estimated and is shown to be negligible under ambient conditions for $BaTiO_3$. Within the electromechanical regime, strong (classical) and weak (field-induced) indentation limits were distinguished. The contribution of different electroelastic constants of the material to the response amplitude was investigated and an almost linear correlation between the piezoresponse and d_{33} was illustrated for a series of PZT materials in the strong-indentation regime. These solutions are represented by contrast mechanism maps that elucidate the effect of experimental conditions on PFM. An approach for simultaneous acquisition of the piezoresponse and surface potential image was developed. These data were shown to be complementary for the general case. Finally, based on these solutions the temperature dependence of the piezoresponse on a $BaTiO_3$ surface was interpreted in terms of a weak-indentation and dielectric-gap model. These solutions can be extended to domains of random orientation and to the analysis of stress effects in thin films by using renormalized effective electromechanical constants. Expressions for the potential and field in the tip-surface junction and in the ferroelectric provide the framework for analyzing polarization switching phenomena and the quantification of local hysteresis loops.

ACKNOWLEDGMENTS

The authors gratefully acknowledge the financial support from NSF Grant No. DMR 00-79909 and NSF Grant No. DMR 00-80863. Discussions with Dr. A. E. Giannakopoulos and Professor Subra Suresh (MIT), Professor Mark Kachanov (Tufts), and Professor M. Cohen (UPenn) are greatly appreciated.

[1] A. Gruverman, O. Auciello, and H. Tokumoto, Annu. Rev. Mater. Sci. **28**, 101 (1998).
[2] S. V. Kalinin and D. A. Bonnell, in *Scanning Probe Microscopy and Spectroscopy: Theory, Techniques and Applications*, edited by D. A. Bonnell (Wiley VCH, New York, 2000), p. 205.
[3] M. Nonnenmacher, M. P. O'Boyle, and H. K. Wickramasinghe, Appl. Phys. Lett. **58**, 2921 (1991).
[4] O. Kolosov, A. Gruverman, J. Hatano, K. Takahashi, and H. Tokumoto, Phys. Rev. Lett. **74**, 4309 (1995).
[5] K. Takata, K. Kushida, K. Torii, and H. Miki, Jpn. J. Appl. Phys., Part 1 **33**, 3193 (1994).
[6] K. Takata, J. Vac. Sci. Technol. B **14**, 882 (1996).
[7] A. L. Gruverman, J. Hatano, and H. Tokumoto, Jpn. J. Appl. Phys., Part 1 **36**, 2207 (1997).
[8] P. Lehnen, J. Dec, and W. Kleemann, J. Phys. D **33**, 1932 (2000).
[9] C. S. Ganpule, V. Nagarjan, H. Li, A. S. Ogale, D. E. Steinhauer, S. Aggarwal, E. Williams, R. Ramesh, and P. De Wolf, Appl. Phys. Lett. **77**, 292 (2000).
[10] A. Gruverman and Y. Ikeda, Jpn. J. Appl. Phys., Part 2 **37**, L939 (1998).
[11] S. Hong, E. L. Colla, E. Kim, K. No, D. V. Taylor, A. K. Tagantsev, P. Muralt, and N. Setter, J. Appl. Phys. **86**, 607 (1999).
[12] E. L. Colla, S. Hong, D. V. Taylor, A. K. Tagantsev, N. Setter, and K. No, Appl. Phys. Lett. **72**, 2763 (1998).
[13] J. A. Christman, S. H. Kim, H. Maiwa, J. P. Maria, B. J. Rodriguez, A. I. Kingon, and R. J. Nemanich, J. Appl. Phys. **87**, 8031 (2000).
[14] K. Takata, H. Miki, K. Kushida-Abdelghafar, K. Torii, and Y. Fujisaki, Appl. Phys. A: Mater. Sci. Process. **66**, S441 (1998).
[15] A. Gruverman, O. Auciello, and H. Tokumoto, Appl. Phys. Lett. **69**, 3191 (1996).
[16] S. V. Kalinin and D. A. Bonnell, J. Appl. Phys. **87**, 3950 (2000).
[17] E. Z. Luo, Z. Xie, J. B. Xu, I. H. Wilson, and L. H. Zhao, Phys. Rev. B **61**, 203 (2000).
[18] V. Likodimos, M. Labardi, and M. Allegrini, Phys. Rev. B **61**, 14 440 (2000).
[19] S. V. Kalinin and D. A. Bonnell, Appl. Phys. Lett. **78**, 1116 (2001).
[20] J. Munoz-Saldana, G. A. Schneider, and L. M. Eng, Surf. Sci. **480**, L402 (2001).
[21] M. Alexe, A. Gruverman, C. Harnagea, N. D. Zakharov, A. Pignolet, D. Hesse, and J. F. Scott, Appl. Phys. Lett. **75**, 1158 (1999).
[22] A. L. Roytburd, S. P. Alpay, V. Nagarajan, C. S. Ganpule, S. Aggarwal, E. D. Williams, and R. Ramesh, Phys. Rev. Lett. **85**, 190 (2000).
[23] C. S. Ganpule, A. Stanishevsky, S. Aggarwal, J. Melngailis, E. Williams, R. Ramesh, V. Joshi, and C. Paz de Araujo, Appl. Phys. Lett. **75**, 3874 (1999).
[24] M. Alexe, C. Harnagea, D. Hesse, and U. Gosele, Appl. Phys. Lett. **75**, 1793 (1999).
[25] S. V. Kalinin and D. A. Bonnell, Phys. Rev. B **63**, 125411 (2001).
[26] C. Durkan, M. E. Welland, D. P. Chu, and P. Migliorato, Phys. Rev. B **60**, 16 198 (1999).
[27] C. Durkan, D. P. Chu, P. Migliorato, and M. E. Welland, Appl. Phys. Lett. **76**, 366 (2000).
[28] K. Lee, H. Shin, W. K. Moon, J. U. Jeon, and Y. E. Park, Jpn. J. Appl. Phys., Part 2 **38**, L264 (1999).
[29] C. S. Ganpule, V. Nagarjan, H. Li, A. S. Ogale, D. E. Steinhauer, S. Aggarwal, E. Williams, R. Ramesh, and P. DeWolf, Appl. Phys. Lett. **77**, 292 (2000).
[30] A. Gruverman, Appl. Phys. Lett. **75**, 1452 (1999).
[31] J. W. Hong, K. H. Noh, S. I. Park, S. I. Kwun, and Z. G. Kim, Rev. Sci. Instrum. **70**, 1735 (1999).
[32] J. W. Hong, K. H. Noh, S. I. Park, S. I. Kwun, and Z. G. Kim, Phys. Rev. B **58**, 5078 (1998).
[33] L. M. Eng, H.-J. Guntherodt, G. A. Schneider, U. Kopke, and J. Munoz Saldana, Appl. Phys. Lett. **74**, 233 (1999).
[34] L. M. Eng, H. J. Güntherodt, G. Rosenman, A. Skliar, M. Oron, M. Katz, and D. Eger, J. Appl. Phys. **83**, 5973 (1998).
[35] A. Roelofs, U. Boettger, R. Waser, F. Schlaphof, S. Trogisch, and L. M. Eng, Appl. Phys. Lett. **77**, 3444 (2000).
[36] V. Likodimos, X. K. Orlik, L. Pardi, M. Labardi, and M. Allegrini, J. Appl. Phys. **87**, 443 (2000).
[37] A. Y. Borisevich, S. V. Kalinin, D. A. Bonnell, and P. K. Davies, J. Mater. Res. **16**, 329 (2001).
[38] T. Tybell, C. H. Ahn, and J. M. Triscone, Appl. Phys. Lett. **75**, 856 (1999).
[39] K. Franke, H. Huelz, and M. Weihnacht, Surf. Sci. **415**, 178–182 (1998).
[40] S. Hong, J. Woo, H. Shin, J. U. Jeon, Y. E. Park, E. L. Colla, N. Setter, E. Kim, and K. No, J. Appl. Phys. **89**, 1377 (2001).
[41] D. Sarid, *Scanning Force Microscopy* (Oxford University Press, New York, 1991).
[42] B. D. Terris, J. E. Stern, D. Rugar, and H. J. Mamin, Phys. Rev. Lett. **63**, 2669 (1989).
[43] J. D. Jackson, *Classical Electrodynamics* (Wiley, New York, 1998).
[44] M. Cohen (private communication).
[45] E. J. Mele, Am. J. Phys. **69**, 557 (2001).
[46] W. R. Smythe, *Static and Dynamic Electricity* (McGraw-Hill, New York, 1968).
[47] N. N. Lebedev, I. P. Skal'skaya, and Ya. S. Uflyand, *Problems in Mathematical Physics* (Pergamon, New York, 1966).
[48] H. O. Jacobs, P. Leuchtmann, O. J. Homan, and A. Stemmer, J. Appl. Phys. **84**, 1168 (1998).
[49] S. Timoshenko and J. N. Goodier, *Theory of Elasticity* (McGraw Hill, New York, 1951).
[50] N. A. Burnham and R. J. Colton, in *Scanning Probe Microscopy and Spectroscopy: Theory, Techniques and Applications*, edited by D. A. Bonnell (Wiley VCH, New York, 2000), p. 337.
[51] S. V. Kalinin, C. Y. Johnson, and D. A. Bonnell, J. Appl. Phys. (to be published).
[52] V. M. Fridkin, *Ferroelectric Semiconductors* (Consultants Bureau, New York, 1980).
[53] H. J. Ding, P. F. Hou, and F. L. Guo, Int. J. Solids Struct. **37**, 3201 (2000).
[54] V. Z. Parton and B. A. Kudryavtsev, *Electromagnetoelasticity* (Gordon and Breach, New York, 1988).
[55] A. E. Giannakopoulos and S. Suresh, Acta Mater. **47**, 2153 (1999).
[56] S. A. Melkumyan and A. F. Ulitko, Prikl. Mekh. Tekh. Fiz. **23**, 44 (1987).
[57] E. Karapetian, I. Sevostianov, and M. Kachanov, Philos. Mag. B **80**, 331 (2000).
[58] S. V. Kalinin and D. A. Bonnell, in *Ferroelectric Thin Films IX*, edited by P.C. McIntyre *et al.*, Mater. Res. Soc. Symp. Proc. No. **655** (Materials Research Society, Pittsburgh, 2001).

[59] *Ferroelectrics and Related Substances*, edited by K.-H. Hellwege and A. M. Hellwege, Landolt-Börnstein New Series Vol. 16a (Springer-Verlag, Berlin, 1981).
[60] D. Berlincourt, in *Ultrasonic Transducer Materials*, edited by O. E. Mattiat (Plenum, New York, 1971).
[61] Y. Xu, *Ferroelectric Materials and Their Applications* (North-Holland, Amsterdam, 1991).
[62] This analysis does not take into account the effect of buckling oscillations of the cantilever (to be reported elsewhere).
[63] A. Gruverman, A. Kholkin, A. Kingon, and H. Tokumoto, Appl. Phys. Lett. **78**, 2751 (2001).
[64] M. Abplanalp, J. Fousek, and P. Gunter, Phys. Rev. Lett. **86**, 5799 (2001).
[65] G. Zavala, J. H. Fendler, and S. Trolier-Mckinstry, J. Korean Phys. Soc. **32**, S1464 (1998).
[66] J. A. Christman, R. R. Woolcott, A. I. Kingon, and R. J. Nemanich, Appl. Phys. Lett. **73**, 3851 (1998).
[67] K. Franke, H. Huelz, and M. Weihnacht, Surf. Sci. **416**, 59 (1998).
[68] A. F. Devonshire, Philos. Mag. **40**, 1040 (1949).
[69] A. F. Devonshire, Philos. Mag. **42**, 1065 (1951).
[70] M. Abplanalp, Ph. D. thesis, Swiss Federal Institute of Technology, Zurich, 2001.
[71] C. Harnagea, Ph. D. thesis, Martin-Luther-Universität Halle Wittenberg, Halle, 2001.
[72] S. V. Kalinin and D. A. Bonnell (unpublished).
[73] S. Cunningham, I. A. Larkin, and J. H. Davies, Appl. Phys. Lett. **73**, 123 (1998).
[74] M. Saint Jean, S. Hudlet, C. Guthmann, and J. Berger, Phys. Rev. B **56**, 15 391 (1997).
[75] T. Tybell, C. H. Ahn, and J.-M. Triscone, Appl. Phys. Lett. **75**, 856 (1999).
[76] X. Q. Chen, H. Yamada, T. Horiuchi, K. Matsushige, S. Watanabe, M. Kawai, and P. S. Weiss, J. Vac. Sci. Technol. B **17**, 1930 (1999).
[77] X. Chen, H. Yamada, T. Horiuchi, and K. Matsushige, Jpn. J. Appl. Phys., Part 1 **38**, 3932 (1999).
[78] S. V. Kalinin and D. A. Bonnell (unpublished).